

Optical and spin properties of nitrogen vacancy centers formed along the tracks of high energy heavy ions

Wei Liu*,¹ Aleksi A. M. Leino,² Arun Persaud,¹ Qing Ji,¹ Kaushalya Jhuria,¹ Edward S. Barnard,³ Shaul Aloni,³ Christina Trautmann,^{4,5} Marilena Tomut,^{6,7} Ralf Wunderlich,^{1,8} Hunter Ocker,⁹ Nishanth Anand,⁹ Zhao Hao,⁹ Flyura Djurabekova,² and Thomas Schenkel¹

¹*Accelerator Technology and Applied Physics Division, Lawrence Berkeley National Laboratory, Berkeley, CA 94720, USA*

²*Helsinki Institute of Physics and Department of Physics, University of Helsinki, PO Box 43 (Pietari Kalmin katu 2), 00014, Helsingin yliopisto, Finland*

³*Molecular Foundry, Lawrence Berkeley National Laboratory, Berkeley, CA 94720, USA*

⁴*GSI Helmholtzzentrum für Schwerionenforschung, Planckstraße 1, 64291 Darmstadt, Germany*

⁵*Technische Universität Darmstadt, Institute of Materials Science, Peter-Grünberg-Straße 2, 64287 Darmstadt, Germany*

⁶*GSI Helmholtzzentrum für Schwerionenforschung GmbH, Planckstraße 1, 64291 Darmstadt, Germany*

⁷*Institute of Materials Physics, WWU Münster, Wilhelm-Klemm-Straße 10, 48149 Münster, Germany*

⁸*Faculty of Physics and Earth System Sciences, Felix Bloch Institute for Solid State Physics, Applied Quantum Systems, Leipzig University, Linnéstraße 5, 04103 Leipzig, Germany*

⁹*Earth and Environmental Sciences, Lawrence Berkeley National Laboratory, Berkeley, CA 94720, USA*

(*Electronic mail: weiliu01@lbl.gov)

(Dated: 7 March 2024)

Exposure of nitrogen doped diamond to high energy, heavy ions induces formation of vacancy related color centers aligned along the trajectories of the ions. Quasi 1D chains of coupled NV centers with lengths of a few tens of microns can be building blocks for quantum information processing and they provide insights into harsh radiation-matter interactions. Here, we report on color center formation in diamond (1 ppm nitrogen) with 1 GeV gold and uranium ions. Using depth-resolved photoluminescence, we observe direct formation of single vacancy related color centers (GR1 centers) along the ion tracks. Mobile vacancies can form NV-centers with native nitrogen atoms during thermal annealing. Molecular dynamics simulations indicate that both isolated vacancies and defect clusters form along ion trajectory through electronic stopping processes, leading to broad color center profiles that range from the sample surface to a depth of about 25 microns. We quantify the spin properties of NV-centers formed by swift heavy ions through optical detection of magnetic resonance (ODMR) and validate the feasibility of using swift-heavy-ion-generated NV^- along quasi 1D chains (for isolated tracks from low fluence irradiations) or in thin sheets of coupled 1D spin chains (formed with higher ion fluences) for NV-based magnetometry and for the exploration of quasi 1D and 2D spin textures in diamond.

Negatively charged nitrogen-vacancy (NV^-) color centers in diamond possess an optical accessible spin-1 triplet ground state with up to millisecond longitudinal relaxation time T_1 and coherence time T_2 at room temperature¹. Optical selective optical transitions enable utilizing negatively charged nitrogen vacancy (NV^-) centers for quantum sensing via optical detected magnetic resonance (ODMR), often with superior sensitivity compared to conventional magnetometers². Thanks to the technical simplicity, radiation robustness, chemically inertness, and nanoscale geometry, diamond-NV sensing can be deployed in harsh radiation, biochemical, and geoscience-related environments³⁻⁶. Enabling control of multiple coupled NV^- centers⁷⁻⁹ is essential to realize a variety of functionalities of diamond-NV architectures and unitary fidelity of quantum protocol operations¹⁰⁻¹⁵. Recent studies indicate self-aligned quasi 1D chains of coupled NV^- centers along a length of several tens of microns. This effect is promising for the development of a novel type of quantum register and a building block for NV-based quantum information processing¹⁶⁻¹⁸. Such quasi 1D chain of NV^- centers can be realized by swift heavy ion (SHI, e.g. 1-2 GeV gold/uranium ions) irradiation of single crystal diamonds, which leads to the conversion of native nitrogen atoms to NV centers along the ion trajectories. Adjusting the nitrogen concentration, and the energy and species of the ions allows engineering the average NV^- spacing on the few nanometer scale along ion trajectories and resulting spin chain on the scale of a tens of microns¹⁹⁻²¹. The quasi 1D aligned NV^- centers are promising for the physical implementation of spin chains, which could also be isolated in a later processing step for studies of Ising model spin dynamics and explorations spin textures, spin transport and spin registers²². Formation of GR1 centers and NV centers in diamond by SHI also supports the development of diamond-based single ion track detectors^{21,23} and methods for directional detection of highly energetic dark matter candidates²⁴. Further, the optical readout of NV centers along ion tracks also enables experimental benchmarking for molecular dynamics (MD) simulations of the interaction between SHI and the diamond lattice²⁵.

In this study, we report on GR1 and NV center generation along the tracks of SHI in diamond and quantify the spin properties of NV-centers. Diamond with 1 ppm N density was chosen in order to suppress decoherence induced by the nitrogen spin bath⁹. By using confocal laser scanning fluorescence microscopy¹⁹, we characterized GR1, NV^0 and NV^- centers and the conversion from GR1's to NV-centers. We show that the NV center formation dynamics by SHI can follow the well established two-step process of vacancy formation followed by capture of mobile vacancies by substitutional nitrogen atoms. The SHI induced vacancies can act as optically active

GR1 centers, when presented as individual isolated neutral vacancies. Vacancies form predominantly along the incoming path of SHI where the electronic stopping power is highest. They can further combine with the nearby nitrogen atoms to form NV centers during the latent track cool down. NV⁻ center formation is further enhanced during thermal annealing after SHI irradiations. The micrometer-resolved optical analysis on the NV formation dynamics provides experimental benchmarking data for Monte Carlo simulations of ion track structures and micro-dosimetric models. We probe the spin properties of SHI-induced NV⁻ via ODMR, which shows that SHI-induced NV⁻ centers along quasi 1D chains or in thin sheets (about 30 μm) can be used for applications in high-sensitivity magnetometry and for studies of spin textures in diamonds. Irradiation with SHI is a method for NV-center formation, complementary to more common irradiation with MeV electrons and protons, with the additional feature of alignment of NV centers along the latent tracks of SHI with lengths of tens of microns.

Type IIa diamonds (Element 6) were used in this study with about 1 ppm nitrogen introduced during the chemical vapor deposition growth. $1 \times 10^{13} \text{ cm}^{-2}$ 180 keV Er were implanted into the samples first. One of the purposes of Er implantation²⁶ is to create shallow NV centers at the surface distributed within the top 100 nm as estimated by the stopping and range of ions in matter modeling (SRIM-2008)²⁷. We did not observe optical emission from Er atoms or signatures of NV-Er coupling in optical spectra or in ODMR. Emission from NV-centers near the surface serves as a reference of the sample surface for depth dependent PL measurements. Sample A and sample B were irradiated at the linear accelerator UNILAC at GSI Helmholtzzentrum, Darmstadt, Germany) using 1.1 GeV U ions (a fluence of 1×10^{12} U ions/cm²) and 0.95 GeV Au ions (2.2×10^{12} Au ions/cm²), respectively. Though we used two species of heavy ions in this study, their energy, ranges and the magnitudes of their respective electronic stopping powers were similar (as estimated by SRIM simulations) allowing us to observe common SHI related effects and trends. The samples were covered by a thick honey-comb shaped mask with millimeter sized openings (90% transparency), which allows direct comparison between irradiated and nonirradiated regions during the PL measurements. After irradiation, to enhance the formation of NV⁻ centers, we performed thermal annealing on sample B in two steps and compared the optical properties after the 1st and the 2nd annealing step. The 1st annealing step was for 1 hour at 800 °C in vacuum (10^{-6} mbr), the 2nd annealing step was for 1 hour at 1000 °C in argon atmosphere. We performed secondary ion mass spectrometry (SIMS) measurement on sample B after the thermal annealing steps (See figure S1 in the Supplementary Material). SIMS depth profiles show accumulation of

nitrogen to concentrations of up to $1 \times 10^{19} \text{ cm}^{-3}$ ($\sim 60 \text{ ppm}$) within the top 100 nm depth and then a concentration of $3 \times 10^{16} \text{ cm}^{-3}$ (0.2 ppm), lower than the nominal concentration of 1 ppm indicated by the supplier, Element 6, and also affected by the absolute calibration in SIMS measurements. Er profile is distributed within the 300 nm with an apparent areal density of $4.1 \times 10^{12} \text{ cm}^{-2}$, lower than the nominal implant fluence and potentially affected by the SIMS calibration.

Firstly, we performed depth-dependent PL on sample A (after SHI irradiation with U ions, and without thermal annealing) to characterize the interaction between nitrogen and SHI-formed vacancies along the ion trajectories. Figure 1 (a) shows the PL spectra as a function of the probe depth (refractive index corrected¹⁹) from the surface (marked as red) to the internal depth of $30 \mu\text{m}$ (marked as blue) in the area with SHI irradiation. In the area with Er implantation and without SHI irradiation, we observe a weak GR1 ZPL signal (see figure S2 in the Supplementary Material) that is visible near the sample surface, within the Er ion range. When we probe deeper regions, spectra are dominated by weak emission from native NV^- centers that are present in the as-received sample. The luminescence of GR1 centers is known to originate from individual neutral vacancies²⁸, which evidences that the SHI irradiation generated individual isolated vacancies along the swift ions trajectories by dislodging carbon (or nitrogen) atoms from lattice positions. Meanwhile, weak luminescence from NV^- and NV^0 center can be observed at the ZPLs of 637 nm and 573 nm, respectively. This phenomenon is different from our previous experiment where NV^- centers were preferentially formed in diamond that contained 100 ppm nitrogen following irradiation with SHI ($10^{12} \text{ cm}^{-2} \text{ 1 GeV Au}$)¹⁹. The major difference in the present experiment is the more than 2 orders of magnitude reduced intrinsic nitrogen concentration of 1 ppm, while SHI conditions are similar. Figure 1(b) shows the depth-dependent PL spectrum of sample B in the swift Au irradiated areas after thermal annealing. Here, the spectra are dominated by the typical ZPL of NV^0 at 573 nm and NV^- at 637 nm, with spectral signatures of GR1 centers now absent. The annihilation of GR1 luminescence in sample B after the annealing shows that the SHI-irradiation induced vacancies either combining with nitrogen atoms to form NV centers or annihilated e.g. via recombination with carbon interstitials.

To quantify the PL intensity and analyze conversion between GR1 and NV^- along the swift ion trajectories, Fig. 1 (c) shows an example of deconvolution of the spectra into NV^- and GR1 luminescence component of sample A (at depth = $14 \mu\text{m}$ in the SHI irradiated area)^{29,30}. The deconvolution approach is explained in the Supplementary Material. The GR1 PL intensity is more than one order of magnitude higher than the NV^- intensity after exposure to SHI and be-

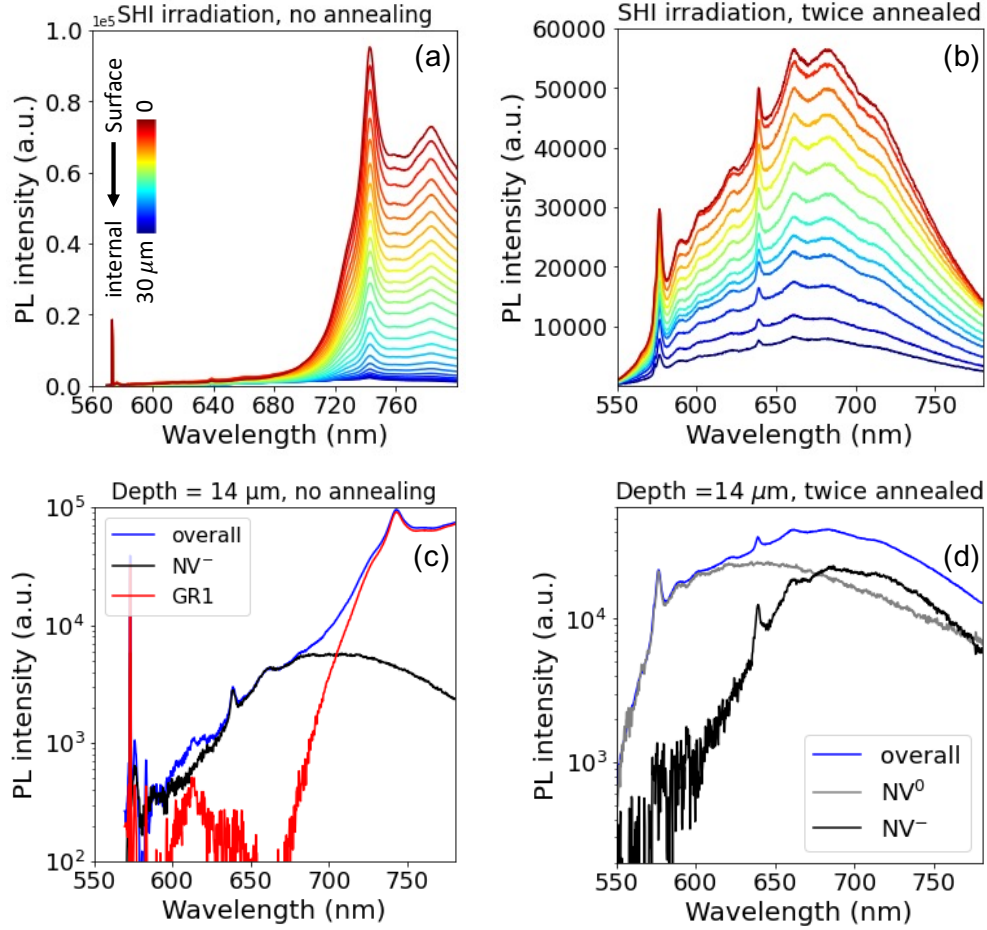


FIG. 1. (a) Color center PL spectrum of sample A (no annealing) as a function of depth from the sample surface to a depth of $30\ \mu\text{m}$ in the area irradiated with 1×10^{12} U ions/ cm^2 fluence of 1.1 GeV energy. (b) Color center PL spectrum of sample B (after two annealing steps) as a function of depth from the sample surface to a depth of $30\ \mu\text{m}$ in the area irradiated with 2.2×10^{12} Au ions/ cm^2 fluence of 0.95 GeV energy. (c) Deconvolution of the PL spectra into NV^- and GR1 luminescence component probed in the SHI irradiated area of sample A at depth = $14\ \mu\text{m}$ (roughly half the SHI range). The red and black spectra show the deconvoluted spectrum resulted from GR1 and NV^- , respectively. The blue spectrum is the full spectrum. (d) Deconvolution of PL spectra of sample B probed in the SHI irradiated area at a depth of $14\ \mu\text{m}$ after annealing. The black and grey spectrum shows the decomposed spectrum resulted from NV^- and NV^0 , respectively.

fore annealing. This indicates that only small portion of SHI-irradiation-created vacancies further combining with nitrogen atom to form NV^- centers at the relatively low nitrogen concentration of nominally 1 ppm. This is in contrast to earlier experiments, where strong NV^- center emission

was observed directly after SHI irradiations and before thermal annealing. At the lower nitrogen concentration, SHI induced vacancies have to move farther to find a nitrogen atom for NV-center formation. At a nitrogen concentration of 100 ppm, the average distance between N atoms is about 5 nm, while it is 20 nm at 1 ppm. Vacancies can diffuse during the cooldown of the (latent) ion track, forming NV's if enough N atoms are present in the track volume and near the track.

As shown in figure 1(d), in the SHI irradiated area, the ratio of the NV^- spectral area to that of NV^0 is enhanced after the 2nd thermal annealing step compared to the 1st annealing step (see figure S3 in the Supplementary Material). NV^0 centers form first during thermal annealing and the charge state balance shifts to NV^- via $NV^0 + e^- \rightleftharpoons NV^-$ during longer annealing times, when vacancy centers dissolve and electrons from the relatively sparse N density can be picked up by thermally activated charge transfer³¹. Performing a 2nd annealing step allows us to thermally drive this process by promoting the ionization of nitrogen donors and to transfer the electron charge to the site of NV^0 centers, consequently converting NV^0 to NV^- .

Figure 2 (a) compares depth profiles of normalized PL intensity of sample A with the GR1 luminescence to that of sample B with dominant NV^- center emissions after annealing. The two PL intensity profiles in figure 2 (a) show a similar plateau up to a depth of 15 μm where the ion energy loss is dominated by electronic stopping process¹⁹. However, at the end of electronic stopping range from 20 to 30 μm depth, the GR1 PL intensity in sample A drops more drastically than the NV^- PL in sample B, presenting two orders of magnitude difference in the GR1 PL intensity between sample surface and the regime of end-of-range ion track. The drastically decrease of GR1 PL intensity at the end of electronic stopping can be related to the clustering of vacancies, which can render them to be optically inactive. The vacancies complexes formation can be further enhanced by nuclear stopping process at end of ion track¹⁹, which causes increase of lattice damage. Differently, in sample B, the reduction of PL intensity of NV^- center emission from sample surface to the end of ion range is less than 1 order of magnitude. We infer that the post annealing convert the extra vacancies into NV^- centers at the end-of-range ion track. These results show that SHI efficiently introduce vacancies along their trajectories in areas of high electronic stopping, in addition to vacancy production at the end of their range where elastic collisions dominate. It also indicates that the NV center formation dynamics by SHI can be governed by a two-step process that depending on the available nitrogen atoms around the track, the SHI-induced vacancies can be in the form of individual neutral vacancies or further combine with the neighboring N to form NV centers. The strong GR1 luminescence introduced directly by SHI irradiation (without thermal

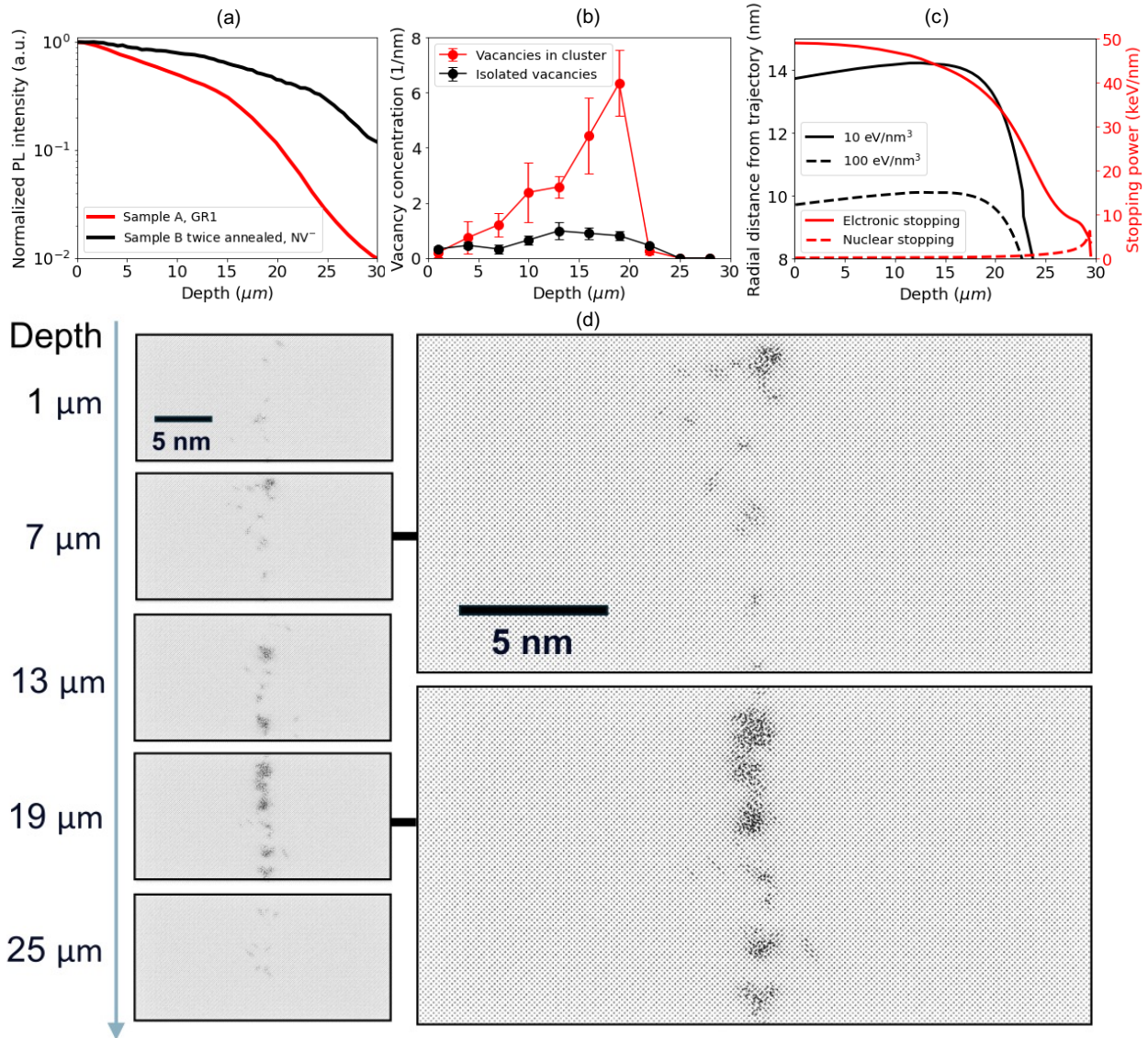


FIG. 2. (a) Comparison of depth-resolved normalized PL intensity (logarithmic scale) of GR1 in sample A (no annealing) and NV^- in the annealed sample B. (b) The simulated concentrations of vacancies in the form of isolated vacancies and vacancy clusters along the ion trajectory from electronic energy loss processes. The contribution from elastic collisions as estimated by SRIM is about 0.5 vacancies/nm in the top 15 microns. (c) Electronic and nuclear stopping powers along the ion trajectory for 1.1 GeV U ions in diamond (right axis). The left axis shows the contour lines of the initial energy density of $10 \text{ eV}/\text{nm}^3$ and $100 \text{ eV}/\text{nm}^3$ after ion impact in the electronic subsystem as estimated as using the delta-ray dose formulas (See supplementary material). (d) Visualization of the MD simulation cells at different depth so that atoms are drawn as gray dots. The arrow on the left shows the ion propagation direction. The left two subfigures show the zoom-in area with defect clusters at 7 μm and 19 μm depth.

annealing) as well as damage repair and re-crystallization via thermal annealing can be unique advantages for applications of diamond as fluorescent nuclear track detector in extreme radiation environments^{20,21}.

To gain insight into vacancy formation resulting from electronic stopping processes for 1.1 GeV U ion, we performed two-temperature MD simulations in pure diamond using the Tersoff potential³². The detailed model is described in Ref.³³ and also in the Supplementary Material. The simulations here exclusively consider the electronic component, omitting nuclear stopping power effects. To circumvent the computation limits, the observed up to 30 μm ion trajectory was segmented into ten small simulations depicting small slabs along the path, each with dimensions of $23 \times 23 \times 11$ nm (XYZ). The trajectory is centered in X and Y directions and penetrates through the cell along the Z axis. Figure 2(b) presents vacancies concentrations along the trajectory determined using the Wigner-Seitz analysis. The plot shows that the concentration of isolated vacancies (Voronoi cells) slightly increase from 0.5 nm^{-1} to 1 nm^{-1} , as the ion track extends from surface to the internal depth of 20 μm . In comparison, the vacancies density in the form of clusters (empty Voronoi cells connected to other cells) increases drastically from 0 to 7 nm^{-1} from the surface to a depth of 20 μm). It is surprising to witness this dramatic increase of vacancy clustering in the range of electronic stopping, while the electronic stopping power decreases monotonically from the surface as shown in 2(c). We tentatively ascribe the enhanced vacancy clustering near 20 μm to the ion velocity effect. Our simulation of the delta-ray radial dose distribution in figure 2(c) reveals that the initial energy density near the trajectory increases due to the decreased velocity of the ion³⁴ until about 20 μm , which leads to strong damage production. Focusing on the role of electronic stopping processes, we exclude contributions to vacancy production from elastic collisions in these summations. From SRIM we estimate the rate of vacancy formation to be ~ 0.5 vacancies/nm from the surface to a depth of 20 microns.

Figure 2(d) shows the visualization atomic disorders along the ion trajectory by the MD simulation at different depth, where atoms are drawn as gray dots. The arrow on the left shows the ion propagation direction. The details of isolated defects and clusters can be seen in the enlarged visualization of the cell at 7 μm and 19 μm depth. The MD simulation results clearly reveal that in the beginning of the ion trajectory (distance to the surface of $< 10 \mu\text{m}$), the damage consists of both isolated interstitial-vacancy (Frenkel) pairs and small defect clusters. The size of the defect clusters tends to gradually increase as the depth of the ion trajectory is greater than 13 μm and less than or equal to 20 μm . In particular, we observe graphitization of the diamond structure showing

amorphous defect clusters near 20 μm depth. In the 20-25 μm range, there is a sharp decrease in the defect concentration, until no defects form at depths greater than 25 μm . Such a velocity effect with graphitization and a sharp decrease of vacancy concentration in the 20-25 μm range can well explain the experimentally observed drastic drop of GR1 emission in this depth range. However, the simulation does not account for nuclear stopping power, due to the calculation complexity. The nuclear stopping power component also becomes significant at the end of the ion ranges, potentially leading to further vacancy defects. Potential synergies of elastic and inelastic energy loss processes on defect kinetics will be explored in future studies³⁵.

We performed ODMR measurements to characterize the electron spin properties of the SHI-induced NV^- after thermal annealing (sample B). The inset in figure 3 shows the example of

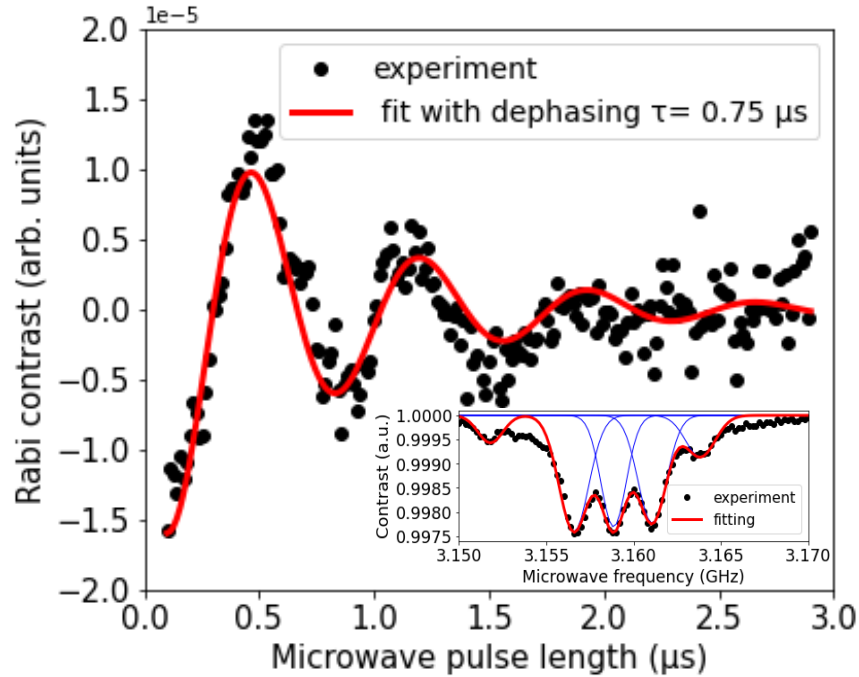


FIG. 3. An example of Rabi oscillations of NV^- spins ($m_s = +1$) probed in the SHI irradiated area of sample B after thermal annealing. The inset shows the ESR signal of the spin state $m_s = +1$ of the NV^- , with an external magnetic field of 100 Gauss was aligned to the $\langle 111 \rangle$ crystallographic orientation. Blue curves correspond to the Gaussian fitted individual resonances, while the red curve corresponds to the accumulative of the fit to multiple resonances.

electron spin resonance (ESR) signal of $m_s = +1$ under 100 Gauss magnetic field, aligned with $\langle 111 \rangle$ crystallographic orientation. It mainly exhibits equal contrast on the three hyperfine reso-

nance lines with a splitting of about 2.2 MHz, which is the typical feature of NV^- electron spins coupled to ^{14}N nuclear spins^{36,37}. The linewidths of the three hyperfine resonance lines is about 1 MHz extracted by Gaussian fitting. The well resolving of ^{14}N hyperfine splitting shows that the SHI approach to NV^- formation preserves a relatively low homogeneous broadening. Additionally, we also observe two well known resonances at both sides of the main peaks with a separation of 12 MHz in Fig. 3(a), and these can be attributed hyperfine interactions with ^{13}C nuclear spins. Fig 3 shows Rabi oscillations of the SHI-induced NV^- ³⁸. We derived an effective dephasing time $\tau = 0.75 \mu\text{s}$ from the decay of amplitude of Rabi oscillation signal, which is comparable to dephasing times reported from NV^- ensembles present in diamonds containing nitrogen concentration in the ppm range^{39,40}. Since the dephasing mechanism of NV^- is mainly governed by the spin bath^{40,41}, the dephasing of NV^- in our sample is affected by a relatively high surface nitrogen concentration as well as other surface charged states. Depth dependent dephasing kinetics can be probed in future studies.

In conclusion, we investigated NV^- center formation dynamics along the trajectories of swift gold and uranium ions in the kinetic energy range of ~ 1 GeV in nitrogen doped diamond. By using confocal laser scanning fluorescence microscopy, we study the interaction between native nitrogen atoms and SHI-induced vacancies during the non-equilibrium process of (latent) ion track formation, and thermal annealing effects on the structural and charge state conversion dynamics between GR1, NV^0 and NV^- centers. We report strong optical emission signals after direct formation GR1 centers along the ion tracks. This direct GR1 formation by SHI through electronic stopping processes can be utilized for the development of diamond-based detectors and methods for dark matter searches with candidates in the extremely high mass range. The NV center formation dynamics by SHI can be a two-step process that is sensitive to the concentration of available nitrogen atoms around the ion trajectory. Molecular dynamics simulations of the diamond lattice subjected to energy deposition through electronic stopping processes from SHI show formation of vacancies. Vacancies can combine with nitrogen atoms in their vicinity forming NV centers during thermal annealing in a well established NV-formation process. MD simulations indicate that that both isolated vacancies and defect clusters form along the ion trajectories. Our simulations further reveal a velocity effect on the rate of vacancy formation that leads to significantly enhanced defect clustering in a depth range where the electronic stopping power is decreasing. We observed that NV^0 is more preferentially formed in diamond with about 1 ppm nitrogen density by SHI excitation, converting to NV^- during consecutive thermal annealing steps. Moreover, we observed an

uplift of NV^- PL profile near the end-of-range of the ions, which indicates additional NV^- centers are activated due to the enhanced nuclear stopping process, providing experimental evidences for future validation of Monte Carlo simulations of ion track structures. We probe the spin properties of the SHI-induced NV^- via ODMR, observing known hyperfine splittings and Rabi oscillations validating that NV^- centers formed by irradiations with SHI are suitable for applications in magnetometry. The presence of NV^- centers in quasi 1D strings along the trajectories of SHI and the formation of 2D sheets of NV^- centers enables studies of spin textures that are complementary to those of NV^- centers formed by more conventional methods, such as irradiation with MeV electrons or protons.

ACKNOWLEDGMENTS

The work is supported by the U.S. Department of Energy Office of Science, Office of Fusion Energy Sciences, under Contract No. DEAC02-05CH11231. Work at the Molecular Foundry was supported by the Office of Science, Office of Basic Energy Sciences, of the U.S. Department of Energy under Contract No. DE-AC02-05CH11231. The ODMR experiments were performed at the geoscience quantum sensing laboratory at Berkeley Lab, supported by the U.S. Department of Energy, Office of Science, Office of Basic Energy Sciences, Chemical Sciences, Geosciences, and Biosciences Division under U.S. Department of Energy Contract No. DE-AC02-05CH11231. The results presented here are based on a UMAT experiment, which was performed at the M-branch of the UNILAC at the GSI Helmholtzzentrum für Schwerionenforschung, Darmstadt (Germany) in the frame of FAIR Phase-0.

DATA AVAILABILITY STATEMENT

The data that support the findings of this study are available from the corresponding author upon reasonable request.

APPENDIXES

Figure S1 shows the layers in sample B after 2ed annealing as measured by SIMS measurement on the depth profile of the native nitrogen and implanted-Er concentration.

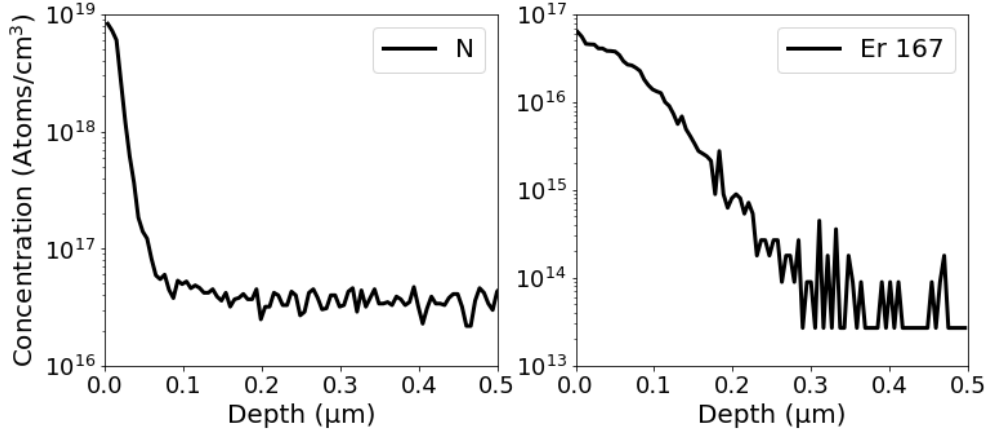


FIG. S1. SIMS measurement of native nitrogen (left) and implanted Er (right) concentration distribution as a function of depth in sample B.

Figure S2 shows the series of PL spectra in the area with only Er implantation and without SHI irradiation of sample A. The spectra probed near the surface (red), where is implanted by Er ions,

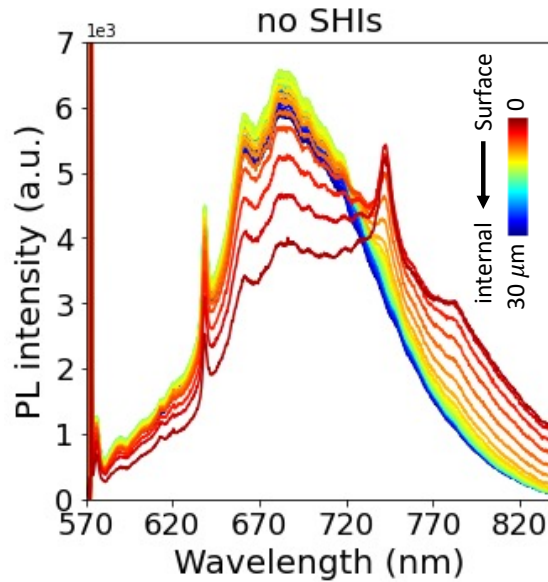


FIG. S2. Depth dependent PL spectrum in the area with only Er implantation and without SHI irradiation of sample A .

reveals stronger GR1 ZPL around 740 nm than the NV^- ZPL at 637 nm. It suggests that GR1 center, as isolated neutral vacancies, tends to be more preferentially formed by Er or other species of heavy ion in the diamond with relative low nitrogen concentration (e.g. 1 ppm). As comparison, as the probing the interior, where beyond the Er ion track range, the spectra (blue) is dominated

by the native NV^- emission.

Deconvolution of spectra: For sample A, the decomposed GR1 spectrum is obtained by subtraction of overall spectrum by an intrinsic NV^- dominated spectrum, which is probed in the internal depth larger than the ion track range. As to sample B, we observed the PL spectra stem from the sample surface are dominated by the NV^0 emission, showing strong 573 nm ZPL and its related phonon side, without appearing any of NV^- ZPL, which can be due to the surface state favorably forming NV^0 . This fortuitous feature allows us to decompose the overall spectrum into NV^0 and NV^- component, separately.

Figure S3 shows the deconvoluted the overall spectrum into NV^- and NV^0 components of the sample B in the SHI irradiated area (after 1st annealing, at depth = 14 μm). We observed that

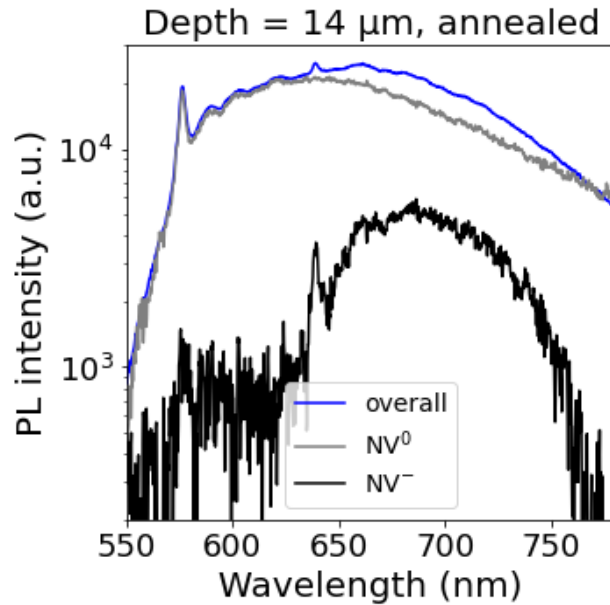


FIG. S3. Deconvolution of PL spectra of sample B probed in the SHI irradiated area at depth = 14 μm by 1st annealing

the NV^0 luminescence is the major component contributed to the overall spectrum, instead of the NV^- , which evidence the higher conversion yield of nitrogen atom to NV^0 by 1st annealing. It is likely due to the limited nitrogen atom (1 ppm) in this sample, which acts as donor to provide electron for NV^- formation. In addition, the parasitic formation of divacancies (V_2) along ion tracks may act as deeper acceptors, which can trap electrons and cause the NV centers mainly as a form of the neutral charge state⁴². Such NV^-/NV^0 ratio variation depending on nitrogen concentration were recently observed in electron-beam irradiated diamond: for the diamond with

a few ppm of nitrogen concentration, electron-beam radiations lead to co-existence of NV^- and NV^0 centers⁴³.

MD-simulations: The two-temperature MD model used for the simulations is the same as in Ref.³³ except for the modification in the electronic heat diffusivity. In Ref.³³, the authors demonstrated the difference between fullerene and gold ions. However, the results revealed a minor deviation in the track formation threshold stopping power for fullerene ions, as a continuous ion track was formed in the simulations at the low velocity regime (0.05 MeV/u), which was, however, not observed experimentally. To improve simulation the accuracy, we adjusted the electronic diffusivity value from 1.3 cm²/s to 2.4 cm²/s, resulting in improved agreement. With the revised value, no continuous ion track is produced at the electronic stopping power 20 keV/nm, whereas a continuous ion track of about 4 nm in diameter forms at 40 keV/nm, which is consistent with the experimental observations. The resulting vacancy and interstitial concentrations in the cell were determined using Wigner-Seitz analysis performed with the Voro++ library⁴⁴ and visualized with the OVITO software⁴⁵. Each simulation is repeated 4 times for statistics. On the other hand, several semi-empirical expressions for the radial dose distribution from delta-rays have developed in the literature^{46,47}. Chunxian et al.⁴⁷ developed a dose formula by combining empirical electron energy-range relation in aluminum with the Rutherford delta-ray production formula. While it was originally developed for microdosimetry, this equation offers a satisfactory level of precision when compared with more complex Monte Carlo simulations also in inorganic materials⁴⁸. The energy density in Fig 2 (d). was estimated using the delta-ray dose formula of Chunxian et al. so that it was normalized with the electronic stopping power at a given depth as predicted by the SRIM 2010 software^{33,48}. The resulting energy density is used in the two-temperature MD model to estimate the initial electronic temperature. Similar approach has been extensively used in prior studies³⁴.

REFERENCES

- ¹L. Rondin, J.-P. Tetienne, T. Hingant, J.-F. Roch, P. Maletinsky, and V. Jacques, “Magnetometry with nitrogen-vacancy defects in diamond,” *Reports on progress in physics* **77**, 056503 (2014).
- ²J. F. Barry, J. M. Schloss, E. Bauch, M. J. Turner, C. A. Hart, L. M. Pham, and R. L. Walsworth, “Sensitivity optimization for nv-diamond magnetometry,” *Reviews of Modern Physics* **92**, 015004 (2020).

- ³T. Zhang, G. Pramanik, K. Zhang, M. Gulka, L. Wang, J. Jing, F. Xu, Z. Li, Q. Wei, P. Cigler, *et al.*, “Toward quantitative bio-sensing with nitrogen–vacancy center in diamond,” *ACS sensors* **6**, 2077–2107 (2021).
- ⁴K.-M. C. Fu, G. Z. Iwata, A. Wickenbrock, and D. Budker, “Sensitive magnetometry in challenging environments,” *AVS Quantum Science* **2**, 044702 (2020).
- ⁵S. Bakhshandeh, “Quantum sensing goes bio,” *Nature Reviews Materials* **7**, 254–254 (2022).
- ⁶G.-Q. Liu, R.-B. Liu, and Q. Li, “Nanothermometry with enhanced sensitivity and enlarged working range using diamond sensors,” *Accounts of Chemical Research* **56**, 95–105 (2023).
- ⁷F. Dolde, I. Jakobi, B. Naydenov, N. Zhao, S. Pezzagna, C. Trautmann, J. Meijer, P. Neumann, F. Jelezko, and J. Wrachtrup, “Room-temperature entanglement between single defect spins in diamond,” *Nature Physics* **9**, 139–143 (2013).
- ⁸A. Jarmola, V. Acosta, K. Jensen, S. Chemerisov, and D. Budker, “Temperature- and magnetic-field-dependent longitudinal spin relaxation in nitrogen-vacancy ensembles in diamond,” *Physical review letters* **108**, 197601 (2012).
- ⁹E. Bauch, C. A. Hart, J. M. Schloss, M. J. Turner, J. F. Barry, P. Kehayias, S. Singh, and R. L. Walsworth, “Ultralong dephasing times in solid-state spin ensembles via quantum control,” *Physical Review X* **8**, 031025 (2018).
- ¹⁰T. H. Taminiou, J. Cramer, T. van der Sar, V. V. Dobrovitski, and R. Hanson, “Universal control and error correction in multi-qubit spin registers in diamond,” *Nature nanotechnology* **9**, 171–176 (2014).
- ¹¹G. Waldherr, Y. Wang, S. Zaiser, M. Jamali, T. Schulte-Herbrüggen, H. Abe, T. Ohshima, J. Isoya, J. Du, P. Neumann, *et al.*, “Quantum error correction in a solid-state hybrid spin register,” *Nature* **506**, 204–207 (2014).
- ¹²X. Rong, J. Geng, F. Shi, Y. Liu, K. Xu, W. Ma, F. Kong, Z. Jiang, Y. Wu, and J. Du, “Experimental fault-tolerant universal quantum gates with solid-state spins under ambient conditions,” *Nature communications* **6**, 8748 (2015).
- ¹³Y. Wang, F. Dolde, J. Biamonte, R. Babbush, V. Bergholm, S. Yang, I. Jakobi, P. Neumann, A. Aspuru-Guzik, J. D. Whitfield, *et al.*, “Quantum simulation of helium hydride cation in a solid-state spin register,” *ACS nano* **9**, 7769–7774 (2015).
- ¹⁴S. Pezzagna and J. Meijer, “Quantum computer based on color centers in diamond,” *Applied Physics Reviews* **8**, 011308 (2021).
- ¹⁵B. Hensen, H. Bernien, A. E. Dréau, A. Reiserer, N. Kalb, M. S. Blok, J. Ruitenber, R. F.

- Vermeulen, R. N. Schouten, C. Abellán, *et al.*, “Loophole-free bell inequality violation using electron spins separated by 1.3 kilometres,” *Nature* **526**, 682–686 (2015).
- ¹⁶T. Tsuji, H. Ishiwata, T. Sekiguchi, T. Iwasaki, and M. Hatano, “High growth rate synthesis of diamond film containing perfectly aligned nitrogen-vacancy centers by high-power density plasma cvd,” *Diamond and Related Materials* **123**, 108840 (2022).
- ¹⁷S. Greengard, “Qubit devices inch toward reality,” *Communications of the ACM* **64**, 11–13 (2021).
- ¹⁸M. Hamilton and L. Nguyen, “Heterogeneous integration technologies for scaled quantum information processing systems,” *IEEE EPS eNews* (2023).
- ¹⁹R. E. Lake, A. Persaud, C. Christian, E. S. Barnard, E. M. Chan, A. A. Bettioli, M. Tomut, C. Trautmann, and T. Schenkel, “Direct formation of nitrogen-vacancy centers in nitrogen doped diamond along the trajectories of swift heavy ions,” *Applied Physics Letters* **118**, 084002 (2021).
- ²⁰S. Onoda, K. Tatsumi, M. Haruyama, T. Teraji, J. Isoya, W. Kada, T. Ohshima, and O. Hanaizumi, “Diffusion of vacancies created by high-energy heavy ion strike into diamond,” *physica status solidi (a)* **214**, 1700160 (2017).
- ²¹S. Onoda, M. Haruyama, T. Teraji, J. Isoya, W. Kada, O. Hanaizumi, and T. Ohshima, “New application of nv centers in cvd diamonds as a fluorescent nuclear track detector,” *physica status solidi (a)* **212**, 2641–2644 (2015).
- ²²S. Bose, “Quantum communication through an unmodulated spin chain,” *Physical review letters* **91**, 207901 (2003).
- ²³M. Akselrod and J. Kouwenberg, “Fluorescent nuclear track detectors—review of past, present and future of the technology,” *Radiation Measurements* **117**, 35–51 (2018).
- ²⁴M. C. Marshall, M. J. Turner, M. J. Ku, D. F. Phillips, and R. L. Walsworth, “Directional detection of dark matter with diamond,” *Quantum Science and Technology* **6**, 024011 (2021).
- ²⁵J. Liu, H. V. Muinos, K. Nordlund, and F. Djurabekova, “Molecular dynamics simulation of the effects of swift heavy ion irradiation on multilayer graphene and diamond-like carbon,” *Applied Surface Science* **527**, 146495 (2020).
- ²⁶J. Cajzl, P. Nekvindová, A. Macková, P. Malinský, J. Oswald, Z. Remeš, M. Varga, A. Kromka, B. Akhetova, R. Böttger, *et al.*, “Erbium luminescence centres in single- and nano-crystalline diamond—effects of ion implantation fluence and thermal annealing,” *Micromachines* **9**, 316 (2018).
- ²⁷J. B. James Ziegler, M.D. Ziegler, “Software website of the stopping and range of ions in

- matter: <http://www.srim.org/index.htm>,” (2008).
- ²⁸S. Subedi, V. Fedorov, S. Mirov, and M. Markham, “Spectroscopy of gr1 centers in synthetic diamonds,” *Optical Materials Express* **11**, 757–765 (2021).
- ²⁹J. Jeske, D. W. Lau, X. Vidal, L. P. McGuinness, P. Reineck, B. C. Johnson, M. W. Doherty, J. C. McCallum, S. Onoda, F. Jelezko, *et al.*, “Stimulated emission from nitrogen-vacancy centres in diamond,” *Nature communications* **8**, 14000 (2017).
- ³⁰M. Solà-Garcia, S. Meuret, T. Coenen, and A. Polman, “Electron-induced state conversion in diamond nv centers measured with pump–probe cathodoluminescence spectroscopy,” *ACS photonics* **7**, 232–240 (2019).
- ³¹T. Lühmann, J. Meijer, and S. Pezzagna, “Charge-assisted engineering of color centers in diamond,” *physica status solidi (a)* **218**, 2000614 (2021).
- ³²J. Tersoff, “Modeling solid-state chemistry: Interatomic potentials for multicomponent systems,” *Physical review B* **39**, 5566 (1989).
- ³³H. Amekura, A. Chettah, K. Narumi, A. Chiba, Y. Hirano, K. Yamada, S. Yamamoto, A. Leino, F. Djurabekova, K. Nordlund, *et al.*, “Latent ion tracks were finally observed in diamond,” *Nature Communications* **15**, 1786 (2024).
- ³⁴Z. Wang, C. Dufour, E. Paumier, and M. Toulemonde, “The sensitivity of metals under swift-heavy-ion irradiation: a transient thermal process,” *Journal of Physics: Condensed Matter* **6**, 6733 (1994).
- ³⁵T. Schenkel, A. Barnes, A. Hamza, D. Schneider, J. Banks, and B. Doyle, “Synergy of electronic excitations and elastic collision spikes in sputtering of heavy metal oxides,” *Physical review letters* **80**, 4325 (1998).
- ³⁶R. Fischer, A. Jarmola, P. Kehayias, and D. Budker, “Optical polarization of nuclear ensembles in diamond,” *Physical Review B* **87**, 125207 (2013).
- ³⁷B. Smeltzer, L. Childress, and A. Gali, “¹³C hyperfine interactions in the nitrogen-vacancy centre in diamond,” *New Journal of Physics* **13**, 025021 (2011).
- ³⁸D. B. Bucher, D. P. Aude Craik, M. P. Backlund, M. J. Turner, O. Ben Dor, D. R. Glenn, and R. L. Walsworth, “Quantum diamond spectrometer for nanoscale nmr and esr spectroscopy,” *Nature Protocols* **14**, 2707–2747 (2019).
- ³⁹O. R. Rubinas, V. Vorobyov, V. Soshenko, S. Bolshedvorskii, V. Sorokin, A. Smolyaninov, V. Vins, A. Yelissev, and A. Akimov, “Spin properties of nv centers in high-pressure, high-temperature grown diamond,” *Journal of Physics Communications* **2**, 115003 (2018).

- ⁴⁰Y. Mindarava, R. Blinder, C. Laube, W. Knolle, B. Abel, C. Jentgens, J. Isoya, J. Scheuer, J. Lang, I. Schwartz, *et al.*, “Efficient conversion of nitrogen to nitrogen-vacancy centers in diamond particles with high-temperature electron irradiation,” *Carbon* **170**, 182–190 (2020).
- ⁴¹F. Feng, W. Zhang, J. Zhang, L. Lou, W. Zhu, and G. Wang, “Optimizing the density of nitrogen implantation for generating high-density nv center ensembles for quantum sensing,” *The European Physical Journal D* **73**, 1–6 (2019).
- ⁴²P. Deák, B. Aradi, M. Kaviani, T. Frauenheim, and A. Gali, “Formation of nv centers in diamond: A theoretical study based on calculated transitions and migration of nitrogen and vacancy related defects,” *Physical review B* **89**, 075203 (2014).
- ⁴³C. Li, Q. Zhang, N. Zhou, C. Zhang, and Z. Yi, “Impacts of nitrogen concentration and electron irradiation fluence on the formation of nitrogen-vacancy defects in diamond,” *Diamond and Related Materials* **132**, 109623 (2023).
- ⁴⁴C. Rycroft, “Voro++: A three-dimensional voronoi cell library in c++,” Tech. Rep. (Lawrence Berkeley National Lab.(LBNL), Berkeley, CA (United States), 2009).
- ⁴⁵A. Stukowski, “Visualization and analysis of atomistic simulation data with ovito—the open visualization tool,” *Modelling and simulation in materials science and engineering* **18**, 015012 (2009).
- ⁴⁶E. Kobetich and R. Katz, “Energy deposition by electron beams and δ rays,” *Physical review* **170**, 391 (1968).
- ⁴⁷Z. Chunxiang, D. Dunn, and R. Katz, “Radial distribution of dose and cross-sections for the inactivation of dry enzymes and viruses,” *Radiation Protection Dosimetry* **13**, 215–218 (1985).
- ⁴⁸A. Leino, S. Daraszewicz, O. H. Pakarinen, K. Nordlund, and F. Djurabekova, “Atomistic two-temperature modelling of ion track formation in silicon dioxide,” *Europhysics Letters* **110**, 16004 (2015).